THE EFFECTS OF LASER FORMING ON SUPERELASTIC NITI SHAPE MEMORY ALLOYS

Paper # P529

Andrew J. Birnbaum, Y. Lawrence Yao

Mechanical Engineering Department, Columbia University
New York, NY 10027

Abstract

This work focuses on application of the laser forming process to NiTi shape memory alloys. While all NiTi shape memory alloys exhibit both superlasticity and the shape memory effect, this study is restricted to a temperature range over which only the superelastic effect will be active. Specifically, this work addresses laser forming induced macroscopic bending deformations, post process residual stress distributions and changes in microstructure. Like traditional ferrous alloys, the laser forming process may be used as a means for imparting desired permanent deformations in superelastic NiTi alloys. However, this process, as applied to a shape memory alloy also has great potential as a means for shape setting "memorized" geometric configurations while preserving optimal shape memory behavior. Laser forming may be used as a monolithic process which imparts both desired deformation as well as controllable material behavior. Characterization of the residual stress field, plastic deformation and phase transformation are carried out numerically and are then subsequently validated via experimental results.

Introduction

Shape memory materials, due to their highly specialized thermo-mechanical behavior have received much attention in recent years. These behaviors include the traditional one way shape memory effect (SME), the superelastic effect and the two-way shape memory effect (TWSME). The mechanism for all three behaviors is rooted in the phase transformation properties of the alloy. In shape memory alloys (SMA's), phase transformation may be accomplished through the introduction of an externally applied stress and/or manipulation of the thermal content of the alloy.

Laser forming is a fairly mature, non-traditional manufacturing process whose effects have been extensively characterized at various size scales for an assortment of materials. The mechanism for deformation is the production of a transient, non-uniform temperature distribution driving local thermal expansion resulting in controllable permanent deformations. Although some work has been conducted on several classes of materials, the vast majority of investigations are restricted to process application for ferrous alloys [1,2,3].

NiTi shape memory alloys are typically produced by, either vacuum induction melting (VIM) or vacuum arc re-melting (VAR) in order to produce a homogeneous nickel-titanium alloy constitution. The solidified ingots are then usually hot-worked if large material reductions are required, and then cold-worked and annealed in order to provide the final product shape, surface finish, refined microstructure and mechanical properties [4]. For most applications however, superelastic strain ranges, active phase transformation temperature, A_f, shape memory and constrained recovery properties are not acceptable at this stage of the process. Typically, extra mechanical/heat treat steps known as shape setting are required to optimize these parameters with respect to the desired "memorized" shape. Shape setting of shape memory alloys typically consists of constraining the cold-worked, semi-finished part in a desired configuration while subjecting it to an appropriate heat treatment in order to achieve desired superelastic and/or shape memory behavior. This method is limited in that the initial ingot geometry as well as the final desired geometry must be fairly simple. Shape setting techniques which are characterized by varying temperature and stress/strain regimes are chosen based on the final desired material parameters as well as the types of geometric features required [5]. For example, parts subjected to an intermediate temperature processing result in larger recoverable strains, whereas low temperature processing tends to increase the repetition lifespan of the recoverable strain lending itself more toward cyclic type application. Lower temperature treatments are also suited to more complex desired geometries, as the stock is typically annealed at higher temperatures after cold working, softening the material [5]. The laser forming process has the potential for avoiding these competing effects as it provides a means for creating complex desired geometries independently of initial mechanical properties due to the fact that it relies on thermal rather

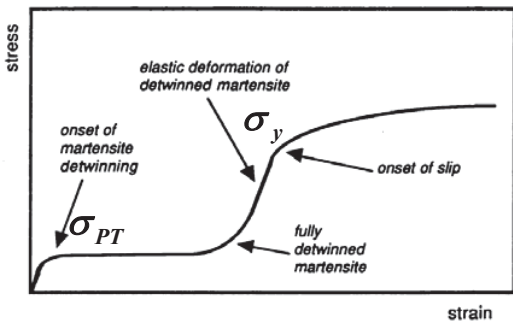

Figure 1: Characteristic constitutive response of NiTi superelastic shape memory alloy in $A_f < T_{operating} < M_d$ [14].

than direct mechanical mechanisms for deformation. It also eliminates the need for hard tooling such as dies and fixtures. Furthermore, due to the inherent local and flexible nature of the process, it may be applied to simple as well as relatively complex initial geometries, as outlined by [6].

Besides the ability to form parts to desired final geometries, the LF process has recently been shown to have potential as a means for training the two-way shape memory effect [7]. The two-way shape memory effect is characterized by a material's ability to "remember" two distinct configurations through thermal stimulation as opposed the traditional shape memory effect which only retains memory of the parent Austenitic phase. Von Busse et. al showed that through multiple pulsed laser forming of NiTi thin foils, one could "train" the formed part to have two distinct configurations that may be activated solely by thermal means. Laser processing of NiTi SMA's have also recently received attention as a means for thin film deposition [8], laser induced actuation [9], laser annealing [10] and laser machining of NiTi SMA components [11].

Process Considerations

While all NiTi shape memory alloys exhibit both the superelastic and shape memory effect, this study is restricted to a temperature range over which only the former will be active. The laser forming process results in an added dimension of material controllability due to its combined thermo-mechanical nature, which is further enhanced by the local and flexible nature of the processing laser. In effect, the laser forming process provides a flexible means for inducing controllable macroscopic deformation, but in synergizing it with SMA's there is the potential for controlling active dynamic properties of the material as well. Specifically, this work addresses laser forming induced macroscopic bending deformations, post process residual stress distributions as well as micro-structural/phase transformation consequences.

The work herein focuses on application of the laser forming process to NiTi shape memory alloys. The driving mechanism for this alloy's distinctive properties is a solid state thermally and/or stress induced diffusionless or thermo-elastic phase transformation. The macroscopic effects of this phase transformation are a vastly enhanced effective elastic loading range (superelastic effect) and an ability to recover inelastic deformations through thermal stimulation (shape memory effect). The two prevalent phases exhibited in NiTi shape memory alloys are the "high" temperature Austenitic or parent phase, and the "low" temperature Martensitic phase. The temperatures at which the alloy will be fully Austenitic or Martensitic are A_f and M_f respectively. The stress induced phase transformation is accomplished by the application of a load such that the critical stress required for transformation is achieved resulting in the formation of stress-induced Martensite (SIM). This is typically performed at temperatures greater than A_f, therefore the initial composition of the alloy is completely Austenite. Upon releasing the load, the reverse transformation occurs resulting in complete elastic recovery. Elastic strains of up to 8-9% have been reported [12]. The so-called R-phase characterized by a rhombohedral microstructure also coexists as a transitional phase during the Austenite to Martensite transformation [13].

The stress/strain response of an Austenitic, superelastic NiTi alloy is shown in Figure 1 [14]. It is seen that upon loading there exists a linear elastic regime with an Austenitic Young's Modulus. This is then followed by a non-linear portion whose start point represents the onset of stress induced phase transformation. The range over which this plateau spans is referred to as the transformation strain. Following this plateau, the sample is fully transformed into stress induced martensite. There then exists another linear elastic range that proceeds with the martensitic Young's Modulus. Beyond that, there exists another non-linear portion representing the yield curve describing permanent slip-type plastic deformation, and finally its ultimate tensile strength.

Another important feature that must be discussed is that the stress required for phase transformation, labelled σ_{PT}, is a positive linear function of temperature. If operating in an Austenitic condition, the stress required to induce phase transformation increases as the operating temperature

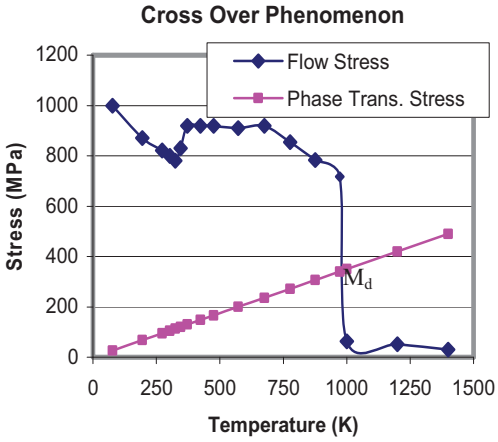

Figure 2: Temperature dependence of flow stress and critical stress required for phase transformation. Note the cross-over phenomenon occurring just below 1000 K where the flow stress becomes lower than the stress required for phase transformation.

increases. The flow stress σ_y, of the alloy is also a function of temperature, although it decreases with increases in temperature. These temperature dependencies become extremely relevant when describing a highly non-uniform thermal process. In fact, at sufficiently high temperatures, there is a temperature, M_d at which the stress to induce phase transformation is higher than that required for plastic deformation. At this point, stress induced phase transformation is no longer possible, and the constitutive response of the alloy takes on the more traditional ferrous alloy appearance with an elastic-plastic response. Fig. 2 is a plot revealing the crossover temperature for the alloy used in the presented experiments based on experimentally determined and literature obtained material properties [15]. This crossover phenomenon adds a considerable amount of complexity to the process analysis, and the implications with respect to the laser forming process are discussed in the numerical approach section.

Experimental Conditions and Setup

Experiments were conducted with a CO_2 laser with a maximum 1500 W power output, with a Gaussian intensity distribution. The laser system remained stationary while a precision XY stage translated the specimens along the desired straight path and velocity (Fig. 3). The Temperature Gradient Mechanism (TGM), which is characterized by a steep

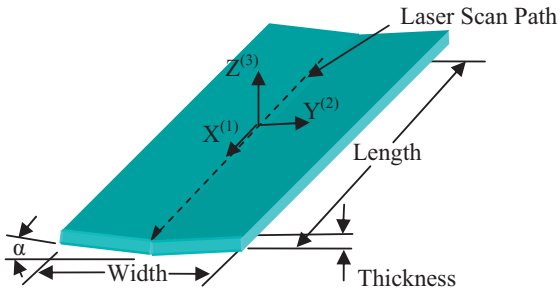

Figure 3: Schematic of laser-specimen experimental setup.

temperature gradient through the thickness of the part, is the dominant mechanism for deformation for all the presented work.

All specimens are rectangular 25 X 50 X 0.61 mm, (width by length by thickness) plate of polycrystalline NiTi (Ni-55.82 Ti-balance (wt.%)), A_f = 5° C (by DSC). Samples surfaces were cleaned with methanol then coated with graphite to enhance laser power absorption. In order to observe microstructural features, all specimens were mechanically polished and then etched in a DI water:HNO_3:HF, 5:4:1 solution. All specimens are subjected to an applied power of 250 W at a beam spot diameter of 7mm, at a velocity of 15 mm/s along a straight scanning path parallel to the edge length. Specimens were subjected to a maximum of 5 laser scans, with ample time given between scans for cooling so as to ensure thermal effects from previous scans would not effect subsequent ones. The scanning direction remained constant, and specimens were cleaned and received a new coating of graphite between each successive scan so as to maintain consistent optical absorption. Subsequent sectioning of the specimens for observation were accomplished with the use of an electric discharge machine (EDM) so as to minimize the introduction of any further stress to due cutting.

Several tensile tests were also conducted in order to calibrate both the elastic-plastic, and superelastic models detailed in the following section. Tensile tests were performed with specimen geometry outlined by ASTM E 8M – 04, according to test procedure outlined in ASTM F2516 – 05. At room temperature, the Young's Modulus of the Austenite and Martensite are 19 GPa and 4 GPa respectively. The upper and lower plateau stresses are 350 MPa and 30 MPa respectively, and the flow stress is approximately 800 MPa.

Numerical Approach

At the current time, numerical implementation of the constitutive response of superelastic shape memory alloys as well as the enhancement of the constitutive models themselves are still under development. DiGiorgi and Saleem [17] provide an extensive review of the constitutive models developed by Tanaka [18], Liang [19] and Lagoudas [20]. Lagoudas' formulation based on a Gibb's free energy approach:

$$G(\sigma,T,\xi,\varepsilon^t) = -\frac{1}{2}\frac{1}{\rho}\sigma:S:\sigma - \frac{1}{\rho}\sigma:[\alpha(T-T_0)+\varepsilon^t] + \ldots$$
$$\ldots c[(T-T_0) - T\ln(\frac{T}{T_0})] - s_0 T + u_0 + f(\xi) \quad (1)$$

has been adopted for use in this work as it is the most physics based model of the three. $\sigma, \varepsilon^t, \xi, T$ and T_0 are the Cauchy Stress Tensor, transformation strain martensitic volume fraction, current temperature and reference temperature respectively. S, α, ρ, c, s_0 and u_0 are the effective compliance tensor, effective thermal expansion tensor density, effective specific heat, effective entropy at reference state and effective internal energy at reference state. The preceding material properties are also calculated via a linear mixture rule:

$$S=S^A+\xi(S^M- S^A),\ \alpha=\alpha^A+\xi(\alpha^M- \alpha^A), \quad (2)$$
$$c=c^A+\xi(c^M- c^A),\ s_0= s_0^A+\xi(s_0^M- s_0^A),$$
$$u_0= u_0^A+\xi(u_0^M- u_0^A)$$

where A and M represent Austenitic and Martensitic properties. The first two terms in equation (1) represent contributions to the energy state from elastic strain energy and the strain energy due to thermal expansion phase transformation. The third term represents the change in internal energy due to changes in temperature. f(ξ) is a hardening function representing the hardening behavior due to phase transformation. Several forms including a trigonometric and logarithmic may be more suited toward specific application, however, the quadratic form

$$f(\xi) = \rho b^M \xi^2 + (\mu_1 + \mu_2)\xi \quad \text{(forward transformation)} \quad (3)$$

$$f(\xi) = \rho b^A \xi^2 + (\mu_1 - \mu_2)\xi \quad \text{(reverse transformation)} \quad (4)$$

is recommended for use with this constitutive model, where ρb^M, μ_1 and μ_2 are strain hardening material constants. The numerical implementation proceeds via a return mapping algorithm by making a prediction through solving the equilibrium and Hookean constitutive equations, and then using the Gibb's formulation as a criteria as to whether or not phase transformation has occurred. There is then a subsequent correction based on the increment in martensitic volume fraction and resulting change in material properties via the above defined rule of mixtures until convergence. A full explanation of the numerical implementation of this constitutive model is available in [21].

ABAQUS has also recently released a subroutine that is capable of simulating the superelastic effect and is phenomenological in nature. Similarly to predicting plastic deformation, it is based on a decomposition of total strain into components stemming from elastic and transformation strain [22]:

$$\Delta\varepsilon^{tot} = \Delta\varepsilon^{el} + \Delta\varepsilon^{tr} \quad (5)$$

The increment in transformation strain is calculated via the stress potential:

$$\Delta\varepsilon^{tr} = a\Delta\xi\frac{\partial F}{\partial\sigma} \quad (6)$$

where ξ is the volume fraction of martensite, a is a material parameter and F and σ are the stress potential and the Cauchy stress tensor respectively. The increment in volume fraction is calculated from the stress potential law:

$$\Delta\xi = f(\sigma,\xi)\Delta F \quad (7)$$

Finally, F is calculated via a linear transformation Drucker-Prager approach:

$$F = \bar{\sigma} - p\tan(\beta) + CT \quad (8)$$

where $\bar{\sigma}$ is the Mises equivalent stress, p the hydrodynamic component of stress, C is a material parameter and T the temperature. Although both of the above mentioned implementations are capable of simulating the superelastic effect, neither combine the superelastic effect with the presence of plastic deformation. This limitation also leads to the inability of simulating the added complexity due to the cross-over phenomenon mentioned in the previous section.

Just to note, ABAQUS has also recently developed a

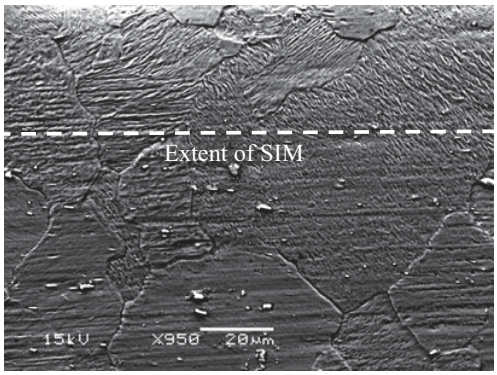

Figure 4: Micrograph of through thickness cross section of five scan specimen (medium magnification, top surface). Note the transition to SIM (Stress Induced Martensite) as the top surface is approached.

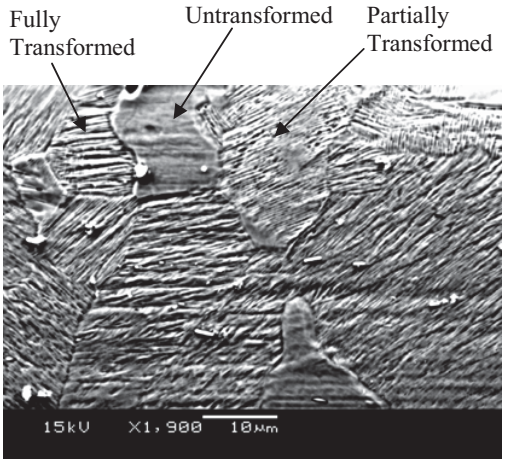

Figure 5: Micrograph of through thickness cross section of five scan specimen (high magnification, top surface). Note the presence of grains of varying extent of transformation.

model that does incorporate the presence of plastic deformation, but can only simulate responses below the crossover temperature.

As an approximation, in order to facilitate simulating both the plastic and superelastic response, the two phenomena are decoupled into an elastic-plastic simulation which predicts plastic deformation, followed by a superelastic simulation predicting local stress induced phase transformation. The former is implemented in the same manner as that of traditional LF modeling techniques [23], i.e. decoupling the

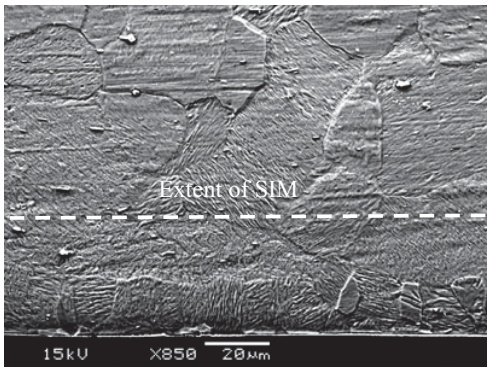

Figure 6: Micrograph of through thickness cross section of five scan specimen (medium magnification, bottom surface). Note the transition to SIM (Stress Induced Martensite) as the bottom surface is approached.

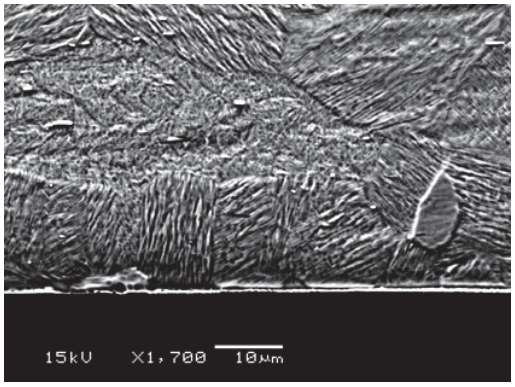

Figure 7: Micrograph of through thickness cross section of five scan specimen (high magnification, bottom surface). Note the presence of SIM (Stress Induced Martensite).

thermal from the mechanical process, and using the thermal results, transient non-uniform temperature distributions, as input to the mechanical model. The justification for this technique is addressed in the following section.

For the thermal model, boundary conditions are as follows: convection is specified on all plate surfaces, while a moving circular heat source with a Gaussian power distribution specified by a user defined FORTRAN script, simulates the effect of the laser. The temperature dependence of thermal

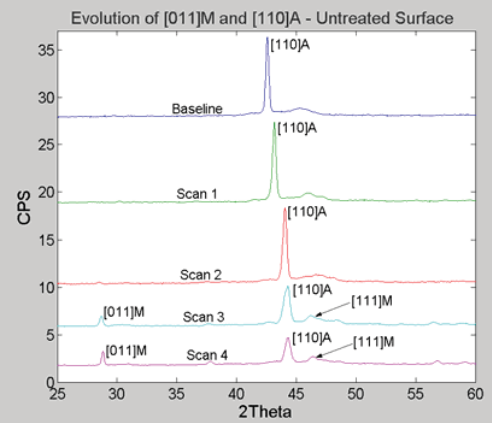

Figure 8: X-ray diffraction spectra over successive scans revealing an increase in martensitic content at the expense of the parent austenitic matrix (untreated surface). (A-Austenite, M-Martensite)

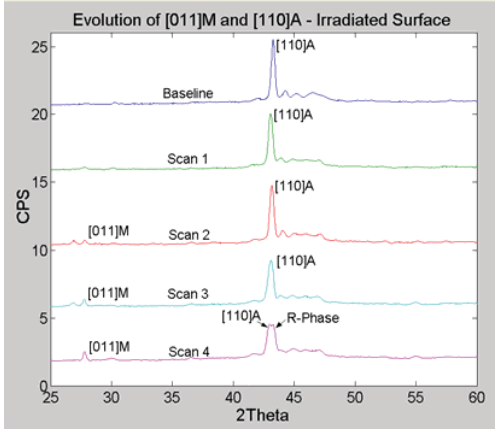

Figure 9: X-ray diffraction spectra over successive scans revealing an increase in martensitic content at the expense of the parent austenitic matrix (irradiated surface). Note the presence of R-Phase in the fourth scan (A-Austenite, M-Martensite)

conductivity and specific heat, obtained from both the material supplier and an extensive review of the available literature [15] is also taken into account.

The mechanical models take into account the non-linear geometric effects stemming from large deformation theory. The temperature dependence of material properties including Young's Modulus, coefficient of thermal expansion and flow stress are taken into account as well. The temperature dependent mechanical properties used have been obtained both from experiment (see experimental setup) and existing literature [15]. The temperature dependence trends have been fit to correspond with the experimentally obtained Austenitic and Martensitic Young's Modulus as well as the flow stress at T=25°C.

Numerical models contain 8,100 20-node quadratic elements; DC3D20 for the thermal case, and C3D20 for the mechanical case in ABAQUS. Attention is given to specifying a fine mesh resolution at and near the scanning path, while away from the scanning path there is a fairly coarse mesh density. Also, as this is model is symmetric about the XZ plane, only half of the geometry is modeled to reduce computation time with the appropriate symmetry boundary conditions at the symmetric plane.

After simulating the thermal field, the resulting temperature distributions are used as inputs to the elastic-plastic mechanical simulation. The elastic-plastic model is then simulated up to time, t_d corresponding to when the temperature has decreased sufficiently such that the stress required for phase transformation is less than the flow stress of the alloy. At this point the displacement field represents deformations due to elastic and plastic deformations only. The resulting displacement field of the entire model, therefore the strain field, is then used as input to the superelastic analysis. The strain field is applied by linearly ramping the displacement at each node over ten seconds to maintain a quasi-static loading configuration. The superelastic analysis is also simulated isothermally at room temperature. This method was chosen due to the recognition that the residual stress and strain fields are due solely to the presence of the locally plastified region in the heat affected zone.

Results and Discussion

Figure 4 is a micrograph obtained via electron microscopy of the plate cross section perpendicular to the laser scanning direction after 5 laser scans. Upon first inspection, no heat affected zone is visible. However, closer inspection of the microstructure near the irradiated and untreated surfaces of the specimen reveal features characteristic of stress induced phase transformation. Figure 5 shows a higher magnified view of the specimen at the irradiated surface near the application of the laser. Martensitic structures are apparent through approximately 40-60 μm depth from the specimen surface. It is also important to note that although laser forming imparts significant thermal energy, the specimen is austenitic at room temperature, and therefore all phase transformation that occurs must

be stress induced as the part is only subjected to

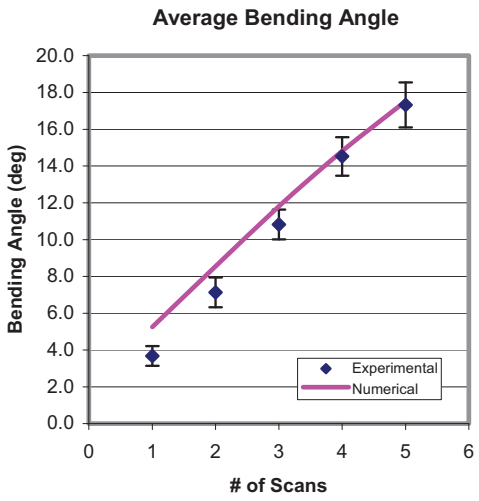

Figure 10: Numerical and experimental average bending angle, P=250 W, v = 15 mm/s, d = 7 mm.

increases in temperature and subsequently cools back to room temperature. Similar results are seen in figures 6 and 7 which show the cross section at the same Y location, but at the untreated of the specimen surface. Again, the depth of transformed crystals is limited to a 20-30 µm layer of material from the untreated surface.

Figures 8 and 9 are x-ray diffraction spectrums taken at representative locations along the laser scan path at the irradiated and untreated surfaces for multiple scans revealing an increase in martensite at the expense of the existing austenitic content as the number of scans is increased. This may be expected as plastic strain increases with each scan increasing the spatial extent of residual stresses whose magnitudes are sufficiently large to induce phase transformation. The formation of the transitional R-phase may also be seen upon the fourth laser scan on the irradiated surface. Currently it is undetermined as to what the relative contributions are to the observed increase in martensitic volume fraction; whether it is due to a further transformation of already transforming grains or increases in residual stress further from the laser scan path leading to the initiation of new grains transforming. This is due to the fact that the volume of material irradiated by the x-rays is on the order of the laser spot size.

Figures 10 and 11 show experimental and numerical results for average bending angle as well as the bending angle distribution along the laser scan path (x-direction). Scans two and four have been omitted

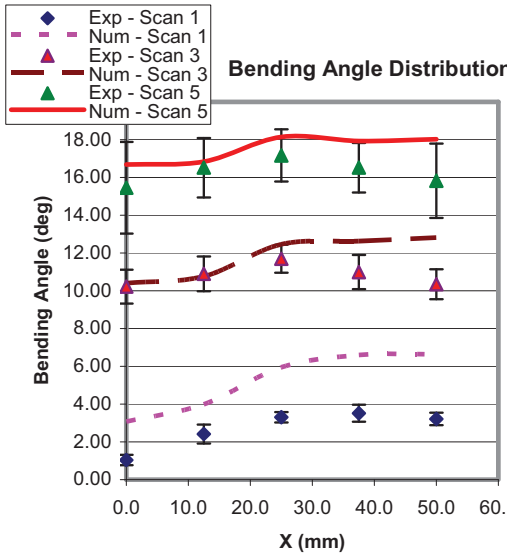

Figure 11: Bending angle distribution along laser scan path for varying numbers of laser scans. P=250 W, v = 15 mm/s, d=7 mm.

from Figure 12 for clarity, but they follow suit in that the discrepancy between the experimental and numerical values decrease as the number of scans increases. A monotonic decrease in relative error is also seen as the number of scans is increased. This is somewhat counterintuitive as one may expect that with each successive scan there is an increase in the volume fraction of martensite and thus the local properties would continue to change resulting in an increasing error due to the fact that the laser forming model is not taking phase transformation into account. However, even with the introduction of further martensite, the application of the laser in successive scans results in a thermally induced martensite to austenite transformation as further plastic deformation occurs resulting in a fully austenitic condition for each scan.

Figure 13 is a contour plot of martensitic volume fraction from the superelastic simulation. It successfully predicts local increases in martensitic volume fraction due to the resulting residual stress field. It shows a monotonic decrease in volume fraction as distance through the thickness and perpendicular to the laser scan is increased. Figure 14shows the numerically predicted average martensitic volume fraction. The average was taken across nodes perpendicular to the laser scan path at a distance equal to the extent of the distance irradiated by the x-ray in the respective experiments. It reveals that both the

irradiated and untreated surfaces have a monotonically

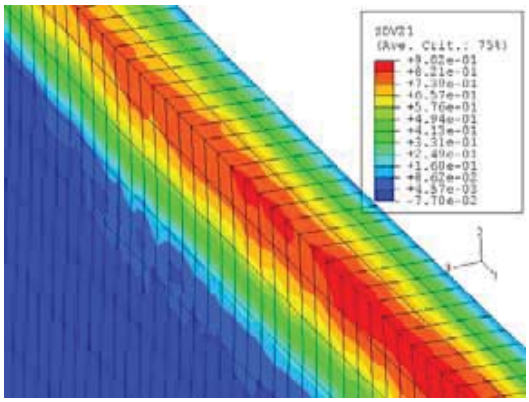

Figure 12: Contour plot of martensitic volume fraction. (P=250 W, v=15 mm/s, d=7 mm)

increasing martensitic volume fraction. This is confirmed via the x-ray diffraction results presented in Figures 8 and 9. However, some discrepancies, particularly with respect to the micrographs in Figures 5 and 7 remain. For example, the micrographs clearly show that the martensitic structures are limited to within fairly shallow depths near the irradiated and untreated surfaces, while the numerical model predicts a fair amount of martensite through the entire thickness. This may be explained as follows. Figure 15 shows the Von Mises, normal X and Y stress

distributions through the specimen thickness predicted by the elastic-plastic laser forming model. Although the quantitative values are clearly not realistic, as this does not take transformation strain into account, the qualitative trends and stress directions do offer some guidance in explaining the above mentioned discrepancies. Due to the nature of the phase transformation models, the change in martensitic volume fraction closely resembles the Von-Mises distributions in both Lagoudas' Gibb's energy formulation and especially the ABAQUS transformation potential approach. Both depend on all components of stress and strain for predicting the resultant volume fraction increment. However, in order to examine the cross section of the specimen, it was sectioned with an EDM. This sectioning results in a new traction free face and must have resulted in the relaxation of the normal stresses in the X direction and the shear stresses τ_{12} and τ_{13}. This relaxation was most likely also accompanied by a reverse phase transformation of stress induced martensite back to austenite. The normal stresses in the Y and Z directions should remain relatively unaffected and therefore the resulting volume fraction distribution should bear more of a resemblance to the Von-Mises

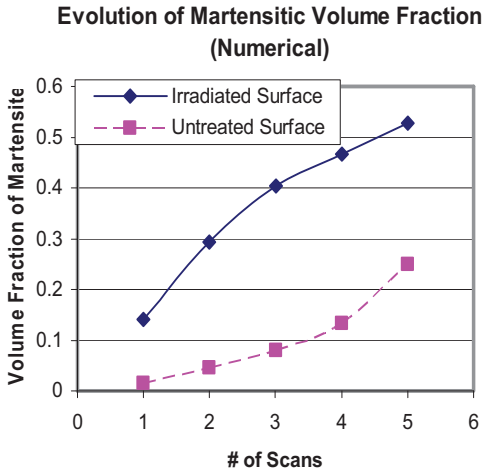

Figure 13: Numerically predicted changes in martensitic volume fraction as a function of the number of laser scans for the irradiated and untreated surfaces.

stress due to the remaining stress components. Referring back to Figure 14, it is seen that S22 decreases monotonically and is tensile at the irradiated surface and compressive at the untreated surface. It is also seen that the magnitudes of S22 are similar on both surfaces and close to zero in the middle. This explains the presence of martensitic structures in an area limited to near both surfaces.

As a first approximation, to facilitate the modeling of the laser forming process, the plastification process and the superelastic response are decoupled. The validity of this approximation is now addressed. Figure 15 shows the temperature and normal plastic strain time history of a representative point on the laser scan path. The laser arrives at that point at t=2.5 sec. Within 0.16 seconds of the laser arrival, the temperature of the point has reached the crossover temperature described in the previous section. At this time, less than 0.3% plastic strain maximum has been generated, suggesting that the constitutive response in close proximity to the laser is solely elastic-plastic with no stress induced phase transformation; and so, during forming the constitutive response including plastic deformation is very much like that of traditional ferrous alloys. The stress induced martensite then forms upon the specimen cooling down to temperatures below the cross-over temperature due to the residual stress field created by the presence of local plastic strain.

As discussed in the numerical approach, the traditional laser forming model is capable of accurately predicting the extent of plastic deformation, but fails to

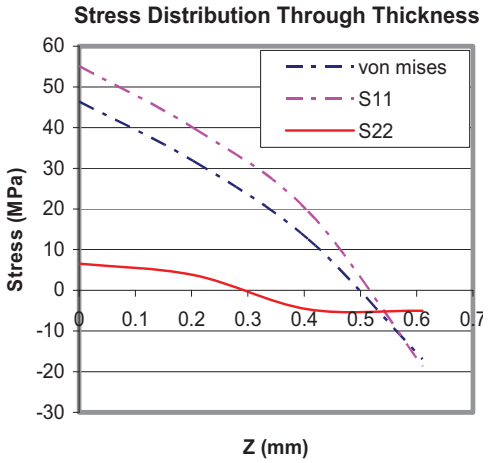

Figure 14: Numerically obtained stress distributions in the X and Y directions as well as the Von Mises through the specimen thickness.

predict the post-process superelastic response of the material. This suggests that the transformation strains upon cooling down are on the same order of magnitude of the plastic strains for lower numbers of scans, but the plastic to transformation strain ratio must also be increasing with respect to increases in laser scans. Although further elastic strains may be produced in the linear martensitic range, micrographs confirm that phase transformation is limited to approximately 40-60 µm and 20-30 µm into the depth for the irradiated untreated surfaces respectively, while the forming model predicts plastic strains on the order of 8% even o.3mm through the depth of the plate. Therefore subsequent scans must result in increases in plastic strain with respect to transformation strains resulting in plastic deformation being the dominant mechanism formacroscopic deformation. This explains the increased model accuracy at higher numbers of scans.

Conclusion

In conclusion, it has been shown that laser forming of shape memory alloys that are austenitic at ambient temperatures does lead to the formation of stress induced martensite due to the post process residual stress resulting from local plastic deformation. Furthermore, it has also been shown that traditional techniques for numerically simulating the laser forming process can accurately predict the macroscopic deformation of specimens, especially in multiple scan applications where plastic deformation is

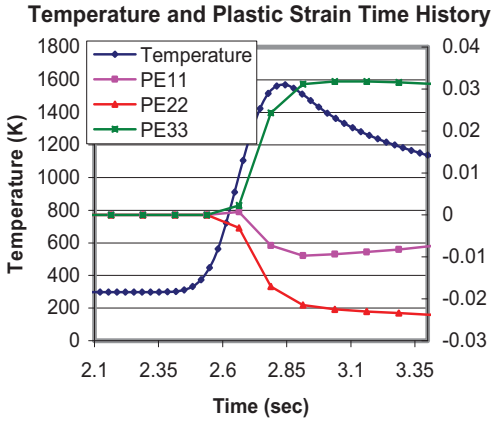

Figure 15: Temperature and plastic strain time history at a representative point on the laser scan path. Laser arrives at t=2.5s.

the dominant mechanism for deformation rather than deformation due to phase transformation.

Traditional shape setting methods require fixture design, a method for constraint, and due to competing factors, there are difficulties in producing complex geometries with optimal shape memory properties concurrently. In the current study, the presence of stress induced martensite has been shown to be local, implying the change in microstructure and macroscopic properties of the overall part remain relatively unaffected. Therefore, the desired shape memory properties may be imparted to the component in a simple initial form such as a plate, tube, foil etc., and then the laser forming process may be used to induce the final desired deformation providing a significant improvement over currently utilized shape setting methods.

Currently, due to the complexities stemming from the process and material itself, the analyses presented are predominantly qualitative in nature. Obtaining quantitative information pertaining to the actual volume fraction of martensite from x-ray diffraction via integrated intensity ratios is not practical due to the aforementioned preferred {110}, the presence of significant plastic deformation resulting in peak widening and R-phase formation resulting in diffracted peaks near Austenitic peaks.

References

[1]Fan, Y., Yang, Z., Cheng, P., Egland, K., and Yao, Y. L., (2005), Numerical and Experimental Investigation of Microstructure Evolution and

Mechanical Behavior of Steel in Laser Forming, *ASME Trans. J. of Manufacturing Science and Engineering*, accepted.
[2]Li, W., and Yao, Y. L., (2000), Numerical and Experimental Study of Strain Rate Effects in Laser Forming, *ASME Trans. J. of Manufacturing Science and Engineering,* Vol. 122, No. 3, pp. 445-451.
[3]Thomson, G. (2001), Material property changes associated with laser forming of mild steel components. *Journal of Materials Processing Technology*, v 118, n 1-3, p 40-44.
[4]Pelton, A., (2003), The physical metallurgy of Nitinol for medical applications *J. of the Minerals, Metals & Materials Society,* v 55, n 5, May, p 33-37.
[5]Otsuka, K., Wayman, C.M. (1998) Shape memory materials, Cambridge University Press.
[6]Cheng, J., and Yao, Y. L., (2004), Process Design of Laser Forming for Three Dimensional Thin Plates, *ASME Trans. J. of Manufacturing Science and Engineering,* Vol. 126, No. 2, pp.217-225.
[7]Ostendorf, A., Paschko, S., Von Busse, A., Bunte, J., Hustedt, M., Fargas, M., (2004), *Proceedings of SPIE - The International Society for Optical Engineering*, v 5662, *Fifth International Symposium on Laser Precision Microfabrication*, pp. 586-592.
[8]Chen, X.Y. Lu, Y.F. Ren, Z.M., Zhang, L., Wang, J.P., Liew, T., (2001), *Materials Research Society Symposium - Proceedings*, v 672, p O10.12.1-O10.12.6.
[9]Zalalutdinov, M., Aubin K., Reichenbach, R., Zehnder A., Houston, B., Parpia, J. and Craighead, H. (2003) Shell-type micromechanical actuator and resonator, *Applied Physics Letters,* Volume 83, Number 18, pp.3815-3817.
[10]Bellouard, Y., Lehnert, T., Clavel, R., Sidler, T., and Gotthardt, R. (2001). Laser Annealing of Shape Memory Alloys: A versatile Tool for Developing Smart Micro-Devices. Journal de Physique IV. Vol. 11 No. 8, pp.8571-8576.
[11]Haferkamp, H., Goede, M., Leester-Schaedel, M. (1999). Keeping the Shape Memory Properties of Miniaturized Components of NiTi-Alloys by Laser Machining. SPIE Conference on Smart Materials Technologies, Vol. 3675, pp. 267-274.
[12]Nemat-Nasser, S. (2006), Superelastic and Cyclic Response on NiTi SMAat Various Strain Rates and Temperatures, *Mechanics of Materials*, v 38, n 5-6, *Shape Memory Alloys*, p 463-474
[13]Miyazaki, S., Kimura, S., Otsuka, K. (1988), Shape-Memory Effect and Pseudoelasticity Associated with the R-Phase Transition in Ti-50at. % Ni Single Crystals. Applied Physics of Condensed Matter, Defects and Mechanical Properties, Vol. 57, No. 3, pp. 467-478.
[14]Turner, T. Thermo-Mechanical Response of Shape Memory Alloy Hybrid Composites. (2001) Langley Research Center.
[15]Jackson, C.M., Wagner, H.J., Wasilewski, R.J. (1972), 55-Nitinol – The Alloy with a Memory: Its Physical Metallurgy, Properties and Applications. NASA.
[16]Cullity, B.D., (1959) Elements of X-Ray Diffraction, Addison Wesley Pub. Co., Reading Mass.
[17]DeGiorgi, V. G. and Saleem, H. (1999). A Review of a Few Shape Memory Alloy Constitutive Models. SPIE Conference on Mathematics and Controls. Vol. 3667, pp. 730-737.
[18]Tanaka, K., Hayashi, T., Itoh, Y. (1992).Analysis of Thermo-Mechanical Behavior of Shape Memory Alloys. J. of Mechanic of Materials.Vol. 13,pp.207-15.
[19]Liang, C. and Rogers, C.A., (1992) A Multi-Dimensional Constitutive Model for Shape Memory Alloys. Journal of Engineering Mathematics, Vol. 26, pp. 153-179.
[20]Boyd, J. and Lagoudas, D.C., (1996). A Thermodynamic Constituive Model for Shape Memory Materials. Part I. The Monolithic Shape Memory Alloy. Int. Journal of Plasticity, Vol. 12, No. 6, pp. 805-842.
[21]Qidwai, M.A., Lagoudas, D.C. (2000), Numerical implementation of a shape memory alloy thermo-mechanical constitutive model using return mapping algorithms, *International Journal for Numerical Methods in Engineering*, v 47, n 6, Feb, p 1123-1168.
[22]Rebelo, N., Walker, N., Foadian, H. (2001), Simulation of Implantable Nitinol Stents, *ABAQUS User's Conference* pp. 1-14.
[23]Birnbaum, A. J., Cheng, P., and Yao, Y. L., (2005), "Effects of Clamping on Laser Forming Process", *ASME J. of Manufacturing Science and Engineering,* accepted.

Acknowledgements

The authors acknowledge the financial support provided by NSF: DMI-0355432 and partial support of NIST: ATP-70NANB2H3031. This work also acknowledges the Columbia MRSEC facility supported via NSF under award: DMR-0213574. Finally, the authors would like to thank Professor Dimitris C. Lagoudas for making the superelastic UMAT subroutine available for use in this work.

Meet the Authors

Andrew J. Birnbaum is currently a doctoral student at the Manufacturing Research Laboratory at Columbia University. B.S and M.S. Carnegie Mellon University.

Dr. Y. Lawrence Yao is currently department chair of Columbia University's Mechanical Engineering Department and director of the Manufacturing Research Laboratory. He received his Ph.D. from the University of Wisconsin-Madison in 1988. He also serves on the Board of Directors of LIA.